OPEN

Tunable large free spectral range microring resonators in lithium niobate on insulator

Inna Krasnokutska [ID], Jean-Luc J. Tambasco & Alberto Peruzzo [ID]

Microring resonators are critical photonic components used in filtering, sensing and nonlinear applications. To date, the development of high performance microring resonators in LNOI has been limited by the sidewall angle, roughness and etch depth of fabricated rib waveguides. We present large free spectral range microring resonators patterned via electron beam lithography in high-index contrast Z-cut LNOI. Our microring resonators achieve an FSR greater than 5 nm for ring radius of 30 μm and a large 3 dB resonance bandwidth. We demonstrate 3 pm/V electro-optic tuning of a 70 μm-radius ring. This work will enable efficient on-chip filtering in LNOI and precede future, more complex, microring resonator networks and nonlinear field enhancement applications.

Microring resonators are fundamental components in any high-index contrast photonic platform[1,2]. They are a highly sought after cavity component, as they enable on-chip field enhancement as well as spectral filtering and fast modulation of optical signals[1,3–6]. In the past decade, microring resonators have been demonstrated in a multitude of platforms including silicon (Si)[7,8], silicon nitride (SiN)[9], aluminium nitride (AlN)[10,11], galium arsenide (GaAs)[12,13] and indium phospide (InP)[14]. The applications of microring resonators are vast, ranging from sensing biological samples[15], to filtering and demultiplexing telecommunication lines[3,13], and generating frequency combs for spectroscopy[16].

Microring resonators are challenging photonic components to fabricate, as losses incurred in the cavity are greatly amplified. To achieve a large free spectral range (FSR) for telecommunication applications and sensing, small, single-mode high-index contrast waveguides are required. Microring resonators can also be cascaded to increase the spectral enhancement, or create various types of filters[17] and this requires very precise and careful control of the 3 dB resonance bandwidth and FSR[9]. In general, a ring performance is limited either by the material properties, such as 2-photon absorption in the C-band of Si, or the ability to nanostructure the material to produce small waveguides with smooth sidewalls.

Lithium Niobate (LN) could greatly benefit from microring resonators to enhance efficiency of nonlinear optical and electro-optic (EO) phenomena, as well as prepare it for telecommunication use. Traditionally, LN has only supported prohibitive low-index contrast (0.01–0.04) waveguides made by Ti indiffusion (Ti:LN)[18] and annealed/soft proton exchange (APE/SPE:LN)[19,20]. There exists further techniques including traditional proton exchange (PE)[21], as well as specialized PE techniques including high index soft proton exchange (HISoPE)[22] or high vacuum proton exchange (HiVacPE)[23], which enable higher index contrast waveguides (0.04–0.14); however, the performance of these waveguides are often compromised due to destroyed nonlinearities and increased propagation loss. With the commercialization of Lithium Niobate On Insulator wafers (LNOI)[24], waveguides with a high-index contrast (~0.5) can now be realized in LN. Small radius, multimode waveguide rings have been reported in LNOI, but suffered from high propagation loss due to fabrication imperfection[24,25]. Recent improvement in the fabrication process has led to reduced sidewall roughness, enabling the fabrication of ultra-low loss waveguides[26,27] and microring resonators with extremely high Q-factors[26]. Due to the complex nature of processing LNOI, low-loss, single-mode, compact rings (down to 30 μm of radius) in LNOI with a high FSR are yet to be reported. Due to the complex chemistry of etching LNOI, most etching processes result in ~50° sidewall angle waveguide[28,29], hampering the ability to produce small gaps, which are critical in the fabrication of grating couplers, compact directional couplers and multistage microring resonator filters; however, this problem was recently solved where ~75° sidewall angle waveguides were reported[27].

Quantum Photonics Laboratory and Centre for Quantum Computation and Communication Technology, School of Engineering, RMIT University, Melbourne, Victoria, 3000, Australia. Inna Krasnokutska and Jean-Luc J. Tambasco contributed equally. Correspondence and requests for materials should be addressed to A.P. (email: alberto. peruzzo@rmit.edu.au)

1

The tuning and reconfigurability of photonic components is a necessity for many practical applications. Tunable rings resonators have been reported in several photonic platforms, including Si, which achieve a high-speed modulation via carrier-depletion and thermal wavelength tuning via resistive heaters[30]. However, carrier depletion suffers from increased optical absorption and a limited response time, restricting the performance of high-speed switches. Electro-optics offers a solution to these challenges, and has been demonstrated in Si on LN[31,32], AlN[33] and LNOI[34–36]. The devices reported to date in Z-cut LNOI have either required two-step laser lithography[35] or had performance challenges due to the waveguides being multimode and having limiting propagation losses[36].

In this work, we present a detailed study of all-pass microring resonators fabricated monolithically in Z-cut LNOI from small, low-loss, high-index contrast and single mode C-band waveguides. We analyze the performance of multiple rings with varying radii from $30\,\mu$m to $90\,\mu$m. The demonstrated heavily overcoupled microring resonators have a maximum FSR of 5.7 nm and a large 3 dB resonance bandwidth that both agree well with the design and simulation. In contrast to previous work who focused on reaching high Qs, this work aims at filtering applications where strong coupling between the ring and bus-waveguide is desired which results in a larger bandwidth of the cavity resonance and a reduced Q correspondingly. Furthermore, we demonstrate the versatility of our fabrication process, etching down to 300 nm trenches in LNOI, critical for advanced photonic components. We further report 3 pm/V electro-optic tuning of a $70\,\mu$m-radius microring resonator—to the authors' knowledge, this is the largest to date in Z-cut LNOI. We expect the microring resonators in this work to pave the way towards on-chip filtering in LNOI with ring networks, as well as field enhancement applications such as switching and nonlinear photon generation.

Design and Fabrication

Microring resonators with radii 30–90 μm were designed to obtain an FSR from 1.5 to 5.7 nm and were simulated using the commercially available software, Lumerical. Rings of varying radii were fabricated to analyze the FSR and performance for the TE and TM modes. The small bending loss needed for good operation of a 30 μm microring resonator required high-index contrast single mode waveguides at 1550 nm. A mode solver was used to determine the dimensions required to ensure a sufficiently small TM polarization bend radius. The design of the waveguide includes the following parameters: rib height, top width, sidewall angle, refractive indices of the waveguide and claddings, and film thickness. The cross-section of a Z-cut rib waveguide cladded with SiO_2 is shown in Fig. 1(b). The small gap of 300 nm was chosen to heavily overcouple the rings and obtain wide bandwidth resonances, rather than extremely narrow resonances that require very precise wavelength tuning to access. A simulation of the Q-factor as a function of coupling region gap for the TM mode at 1550 nm of a 30 μm microring resonator is shown in Fig. 1(a), and indicates that the 3 dB bandwidth of the microring resonances (FWHM) is $\text{FWHM} = \lambda_{\text{res}}/Q = \sim155$ pm, where λ_{res} is the wavelength of the resonance and Q is the Q-factor. The simulation was performed using Lumerical Mode; the measured losses, as per the Fabry-Perot measurements presented in Fig. 2(a), were taken into account in the simulation model.

The photonic components were fabricated by the process developed and described in our previous work[27]. The process starts with 500 nm thick LN film, which is fabricated using the smart-cut technique on 2 μm of SiO_2 layer and supported by a 500 μm LN substrate. The next fabrication steps rely on electron beam lithography and lift-off of the e-beam evaporated metal layer to obtain a hard mask defining the photonic components. The scanning electron microscopy image (SEM) of a waveguide to a ring coupling region just after the metal lift-off process, is shown in Fig. 1(e). The components were then dry etched in a reactive ion etcher Fig. 1(d). Following etching, the waveguides were cladded with 3 μm thick plasma-enhanced chemical vapor deposition (PECVD) SiO_2. The presented structures were etched deeper than in our previous work to achieve the necessary index contrast, reducing the waveguide bending radius. The rib waveguide cross-section, obtained via focused ion beam (FIB) slicing and scanning electron microscopy (SEM), shows a sidewall angle of 75° and an etch depth of 350 nm Fig. 1(c). Finally, the waveguide facets were diced using optical grade dicing to facilitate butt-coupling. The length of the chip, after all processing steps were completed, is 6 mm.

Experimental Results

In order to confirm that the photonic components are not limited by the propagation loss, loss measurements were performed prior to the characterization of the microrings, using the Fabry-Perot loss measurement technique[37]. Laser light at 1550 nm wavelength is coupled into and out of the polished facets of the waveguide using polarization maintaining (PM) lensed fibers with a mode field diameter of 2 μm. A typical optical transmission spectrum for TM (the TE and TM modes have a similar response) is shown on the Fig. 2(a). Linear inverse tapers 200 μm long down to 200 nm wide tips are used to improve the mode matching between the lensed fibre and the waveguide[38], improving the precision and signal to noise ratio of the Fabry-Perot measurements due to a reduction in the waveguide effective refractive index, minimizing back-reflections. As the waveguide narrows, the mode field diameter at the input and output of the waveguide significantly increases, allowing improved mode matching with the mode of the lensed fiber. The total input and output coupling and propagation loss is 8 dB for a 6 mm long chip, compared to the 15 dB loss achieved with the straight waveguide without tapering section. The estimated upperbound propagation loss is less than 0.5 dB/cm for both the TE and TM modes, which is in agreement with the results obtained in our previous work[27]. We obtain stable (repeatable) FP contrast measurements that vary by just $\pm0.15\%$. The slight modulation of transmission spectrum can be attributed to the imperfect tapering.

The fabricated microring resonators were characterized by sweeping the wavelength of the laser between 1530 to 1610 nm and recording their spectral responses with a commercially available high-speed InGaAs photodiode. The laser light was injected into and out of a 6 mm bus-waveguide via PM lensed fibers. To decrease the chance of interference between multiple oscillations inside of the photonic component, the inverse tapering section was
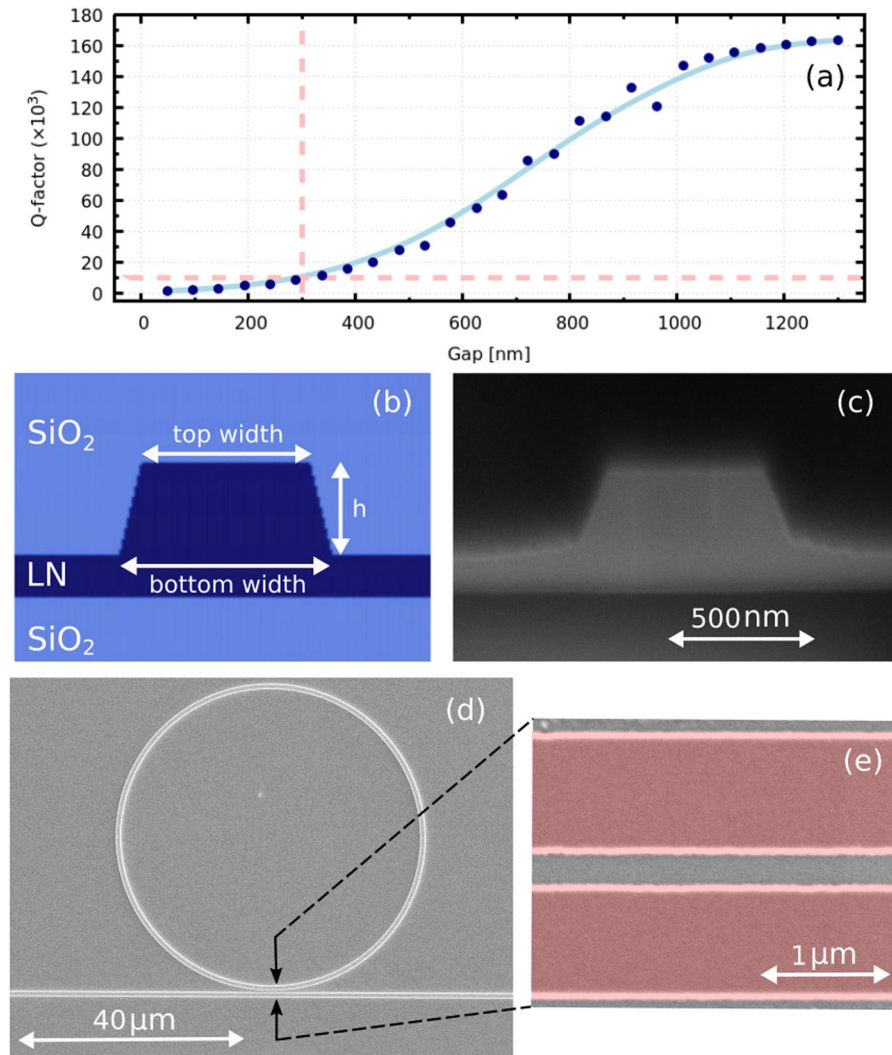
Figure 1. (**a**) Simulation of *Q*-factor as a function of the coupling region gap for a 30 μm radius microring—the light red dashed lines demarcate the simulated *Q*-factor (~10000) for the microring shown in (**d**). (**b**) Design of a single mode LNOI rib waveguide at 1550 nm wavelength; the top width is 650 nm, the bottom width is 840 nm and the waveguide height is 350 nm. Scanning electron microscope pictures: (**c**) cross-section taken by FIB slicing and SEM imaging; (**d**) an etched 30 μm radius ring with a 300 nm gap between the bus waveguide and the ring prior to PECVD SiO$_2$ cladding; (**e**) false-color image of the coupling region after the lift-off process and prior to etching; the false-red highlights the metal etch mask.

not implemented for the microrings—this led to a drop in the mode matching efficiency. We observe that both TE and TM (Fig. 2(b)) modes reaches the largest FSR for the ring with the smallest radius 30 μm; however, the TE and TM modes show different results in terms of the achievable *Q*-factor for this geometry. A *Q*-factor of ~9000 was achieved for the TM mode whilst for the TE mode the *Q*-factor is significantly smaller ~1200. As the radius of the ring increases, the *Q*-factor for TM mode remains almost unchanged (Fig. 2(b)); meanwhile, for the TE mode, it significantly increases (Fig. 2(b)) and the highest *Q*-factor has been achieved for the ring with radius of 90 μm Fig. 2(d). This dissimilarity can be attributed to the difference in the bending loss between both modes. It was deduced by using our numerical model (Fig. 1(a)) and the value of intrinsic quality factor that TM mode bending loss for microring resonator of 30 μm of radius is around 1.5 dB/cm, while for TE mode it estimated to be around 12 dB/cm for the ring with the same radius. By comparing theoretical and experimental results, the effective index for the TE mode is 1.85 and for the TM mode is 1.72 and the TM mode was confined to have an index contrast of ~0.272, whilst the TE mode is lower ~0.247. As the TM mode has a higher index contrast, a smaller bend radius is achieved, enabling smaller microring resonators to be realized. The TE mode bending loss decreased with increasing microring resonator radius, leading to an improvement in the *Q*-factor.

The group indices for the TE and TM modes respectively, n_g^{TE} and n_g^{TM}, are deduced from the fully-vectorial mode solver using the Sellmeier equations for lithium niobate: $n_g^{TM} = 2.33$ and $n_g^{TE} = 2.38$. The FSR can be calculated using FSR $= \lambda^2/(n_g L)$, where L is the circumference of the ring ($L = 2\pi R$), R is the radius of the ring. The simulation curve is plotted with the measured FSR for different microring resonator dimensions in Fig. 3(a,d).
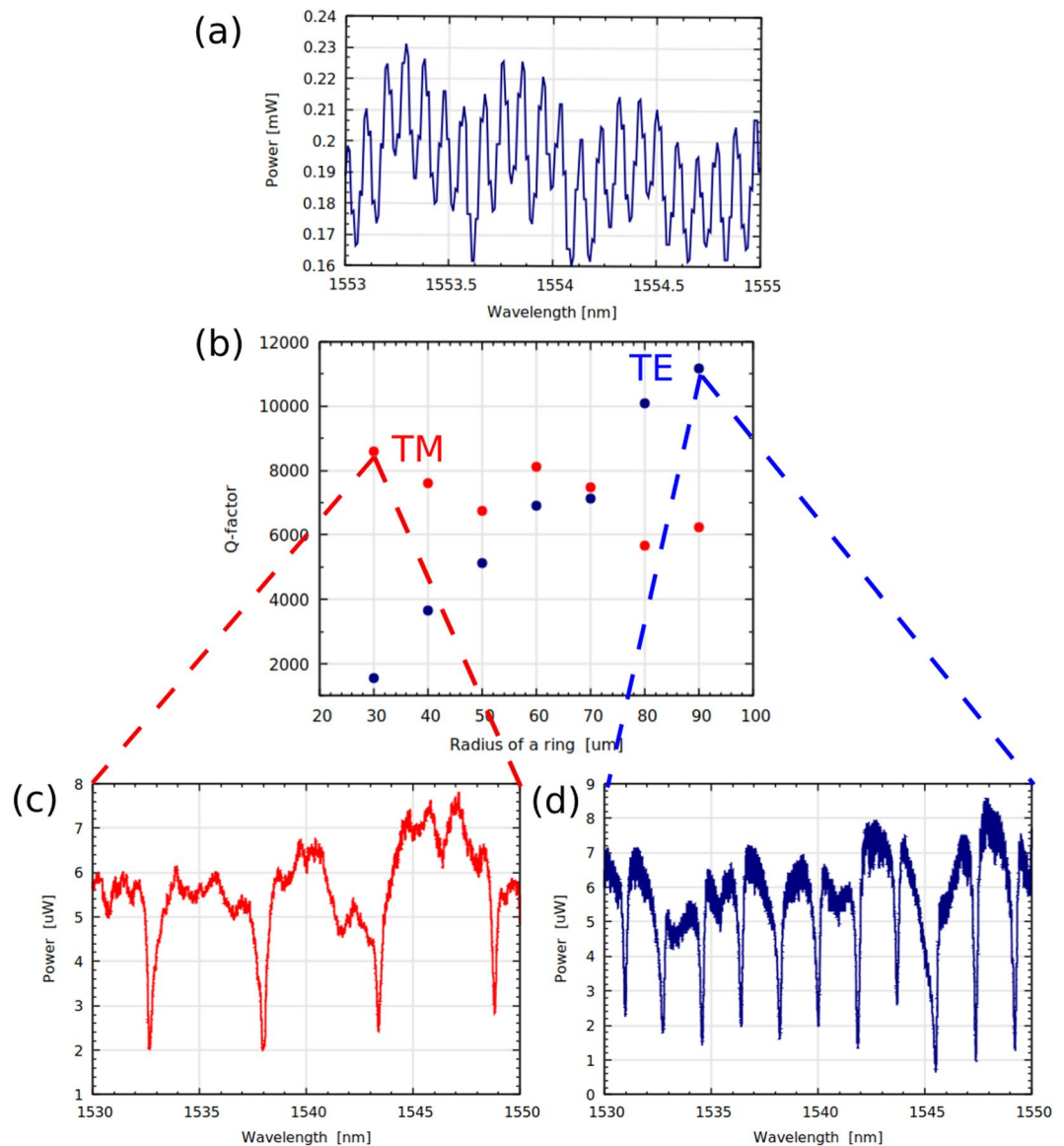
Figure 2. (**a**) Transmission spectrum of the inverse taper with 200 nm width LNOI used for calculating the propagation loss of the TM mode. (**b**) Measured Q-factors of the ring resonators versus their radius for the TE and TM modes. The blue curve corresponds to the TE mode and the red curve corresponds to the TM mode. (**c**) Spectral response of the ring with radius 30 μm for TM mode. (**d**) Spectral response of the ring with radius 90 μm for TE mode.

The simulated E-field distributions of the fundamental waveguide modes at a wavelength of 1550 nm (found using an in-house mode solver) are included to the figures as insets: Fig. 3(b) for the TE mode, and Fig. 3(e) for the TM mode. Also included as insets, Fig. 3(c,f), show the measured power distribution at a wavelength of 1550 nm in a 3×3 μm window; each cell defined by the white grid lines represents a single pixel (a single power measurement). The measured power distribution is performed by sweeping the fiber over the output facet of the waveguide, resulting in a convolution between the fiber mode and the waveguide mode, smearing and enlarging the appearance of the waveguide mode.

Electro-Optic Resonant Wavelength Tuning

An electrode consisting of Cr (20 nm) and Al (500 nm) is deposited directly on the upper cladding of the waveguide. The separation between the electrode and the waveguide is designed to be 3 μm, which is estimated to be close enough that the electric field extending from the electrode can effectively influence the LNOI waveguide, but far enough that the optical loss is not increased. Figure 4(a) shows the simulation result of the static electric potential performed using a finite element solver, with the voltage applied across the top and bottom electrodes. The bottom electrode, serving as a ground plane, is made from Cr (10 nm), Au (100 nm) and Cr (10 nm).

To demonstrate the electro-optic tuning of the devices, we apply a DC voltage from 0 V down to −55 V across the top and bottom electrodes of the microring resonators. The resonance shifts with the applied voltage as shown
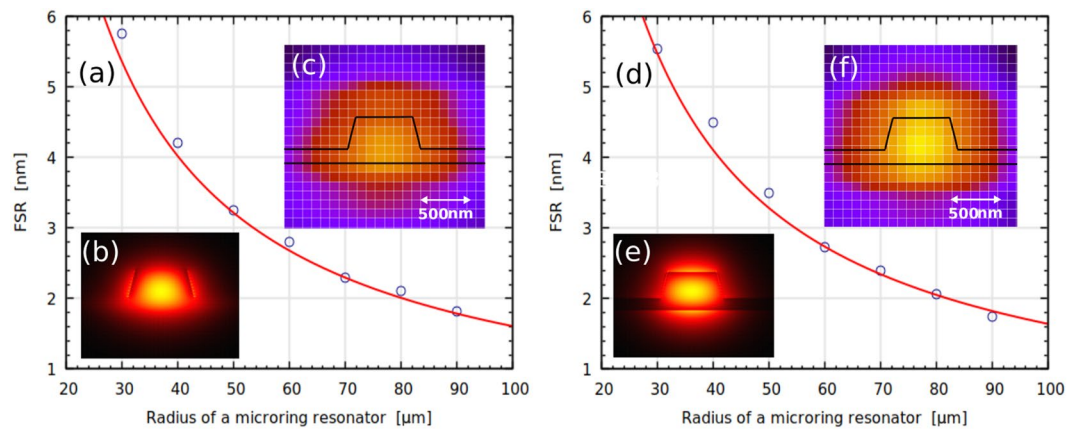
Figure 3. (**a**) Measured FSR as the function of a microring resonator radius for the TE mode and (**d**) for TM mode; the blue circles are measured values, whilst red line is theoretically predicted dependence of FSR on microring resonator radius; (**b**) the simulated electrical field distribution for the TE mode and (**e**) for the TM mode; (**c**) measured optical power distribution at the output of the chip for the TE mode and (**f**) for the TM mode, where black lines schematically show the actual waveguide dimensions.
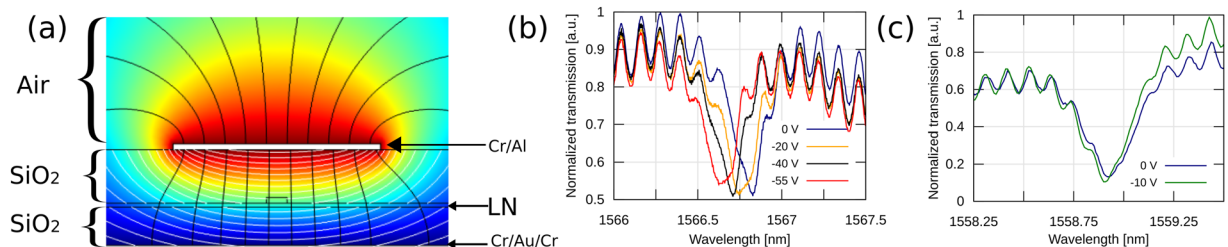
Figure 4. (**a**) Simulation results of electrical field. (**b**) Spectrum of the optical resonances of a 70 μm when voltage from -55 to 0 V is applied. (**c**) Shift in resonance of a 50 μm microring resonator when -10 V is applied.

in Fig. 4(b) corresponding to an average EO tunability of 3 ± 0.04 pm/V. The microring resonators presented in this work show similar tunability; however, it has been observed that microrings with radii ≥ 60 μm experience a DC voltage bias offset—at voltages <20 V, the resonance shifts with tunability <3 pm/V, but at higher voltages, the resonance shifts at average value 3 ± 0.04 pm/V. Meanwhile, rings with radii ≤ 50 μm have a constant tunability of ~ 3 pm/V even at lower voltages (<10 V), as shown in Fig. 4(c). Previous works in LNOI also experience voltage bias offsets; for example, a 50 V bias offset was presented for the same radius (50 μm) microring resonator in[36], making low voltage applications challenging.

Discussion

The Fabry-Perot transmission measurements were conducted on straight waveguides with inverse tapers at both ends and indicate low propagation loss for this platform. The overall insertion loss of the waveguides is dominated by mode-mismatch between waveguide and optical fiber, despite the significant improvement of provided the inverse tapers. Given that the straight waveguides measured have identical dimensions to the waveguides used in the ring resonators and were fabricated on the same chip, the propagation loss in the rings are concluded to be equally low loss.

The demonstrated ring resonators are designed to be strongly overcoupled, increasing their 3 dB resonance bandwidth (and, conversely, reducing their Q-factor). A 300 nm gap in the bus waveguide to microring coupling region provides strong overcoupling. The potential of the nanofabrication process used in this work[27] could be further extended to photonic components including grating couplers and compact directional couplers.

The Q-factor measurements show that it is possible to achieve small and high performance microring resonators for the TM mode—critical for electro-optic and nonlinear applications. Meanwhile, the TE mode bending losses significantly limit the Q-factor of the smaller radius microring resonators; however, increasing the ring radius leads to a substantial increase in Q-factor. It demonstrated that the TM mode can achieve a smaller bend losses than the TE mode, as the index contrast of the TE fundamental mode is less than that of the TM fundamental mode, as verified by both our in-house mode solver, and by the Q-factor simulations conducted in Lumerical Mode for the 30 μm ring.

It was found that the theoretically predicted results for the microring resonators demonstrated in this paper are in a good agreement with the experimental results (Fig. 3). The deviation for n_g is less than 2% leading to precise agreement between the designed and measured FSRs for different ring geometries. Using 350 nm deep ribs, a small TM bend radius was achieved to enable 30 μm TM microring resonators with an FSR of 5.7 nm. The

Material	Radius of a ring (μm)	Q-factor	FSR (nm)	EO tuning (pm/V)
SOI PN junction[30]	7.5	8000	12.6	26
SOI on LN with integrated electrodes[31]	15	11500	7.15	12.5
SOI on LN[32]	15	14000	7.15	3.3
AlN[33]	60	500000	n.a.	0.18
X-cut LNOI[34]	n.a.	50000	n.a.	7
Z-cut LNOI[35]	100	4000	1.66	1.05
Z-cut LNOI[36]	50	2800	3.2	2.15
Z-cut LNOI (this work)	70	7500	2.5	3

Table 1. Comparison between different types of tunable rings.

microring resonators demonstrate a large FSR while maintaining a high coupling coefficient. Previous works have struggled to achieve flexibility in the coupling region due to shallow sidewall angles and further etching challenges. The monolithic lithography presented allows precise engineering of the coupling gap while preserving low sidewall roughness. This result is competitive with other high-index contrast leading platforms, such as SiN and AlN.

For comparison, we report in Table 1 a summary of experimental results on resonant wavelength tuning. It can be seen that tunable ring resonators have been realized in a multitude of photonic platforms. Silicon has reported very high tuning with large FSR[30]. More recent work has shown good performance in hybrid Si on LN, although it requires extra fabrication steps[31,32]. While using AlN has so far resulted in limited tunability[33], LNOI photonics presents a promising approach to tunable ring resonators[34–36].

Conclusion

We have analyzed in detail the performance of large FSR microring resonators in Z-cut LNOI, fabricating rings of varying radii and reporting their characterization for both the TE and TM polarizations. The demonstrated advanced fabrication enables minimal separation (300 nm) between monolithically defined adjacent features, whilst maintaining smooth waveguide sidewalls. We have verified that the optical characteristics of the fabricated microring resonators correspond well with the design and simulation. We have further demonstrated 3 pm/V EO tuning of microrings. These results will precede more complex photonic devices in LNOI, ranging from precise filtering with multistage microring resonators to electro-optically tunable devices, for use particularly in telecommunication, sensing and quantum technology applications.

References

1. Bogaerts, W. *et al*. Silicon microring resonators. *Laser & Photonics Rev.* **6**, 47–73, https://doi.org/10.1002/lpor.201100017 (2012).
2. Vahala, K. J. Optical microcavities. *Nat.* **424**, 839, https://doi.org/10.1038/nature01939 (2003).
3. Xia, F., Rooks, M., Sekaric, L. & Vlasov, Y. Ultra-compact high order ring resonator filters using submicron silicon photonic wires for on-chip optical interconnects. *Opt. Express* **15**, 11934–11941, http://www.opticsexpress.org/abstract.cfm?URI=oe-15-19-11934, https://doi.org/10.1364/OE.15.011934 (2007).
4. Baba, T. *et al*. 50-Gb/s ring-resonator-based silicon modulator. *Opt. Express* **21**, 11869–11876, http://www.opticsexpress.org/abstract.cfm?URI=oe-21-10-11869, https://doi.org/10.1364/OE.21.011869 (2013).
5. Levy, J. S., Foster, M. A., Gaeta, A. L. & Lipson, M. Harmonic generation in silicon nitride ring resonators. *Opt. Express* **19**, 11415–11421, http://www.opticsexpress.org/abstract.cfm?URI=oe-19-12-11415, https://doi.org/10.1364/OE.19.011415 (2011).
6. Hu, Y. *et al*. High-speed silicon modulator based on cascaded microring resonators. *Opt. Express* **20**, 15079–15085, http://www.opticsexpress.org/abstract.cfm?URI=oe-20-14-15079, https://doi.org/10.1364/OE.20.015079 (2012).
7. Xu, Q., Fattal, D. & Beausoleil, R. G. Silicon microring resonators with 1.5-m radius. *Opt. Express* **16**, 4309–4315, http://www.opticsexpress.org/abstract.cfm?URI=oe-16-6-4309, https://doi.org/10.1364/OE.16.004309 (2008).
8. Shi, W. *et al*. Grating-coupled silicon microring resonators. *Appl. Phys. Lett.* **100**, 121118, https://doi.org/10.1063/1.3696082. (2012).
9. Popović, M. A. *et al*. Multistage high-order microring-resonator add-drop filters. *Opt. Lett.* **31**, 2571–2573, http://ol.osa.org/abstract.cfm?URI=ol-31-17-2571, https://doi.org/10.1364/OL.31.002571 (2006).
10. Pernice, W. H., Xiong, C. & Tang, H. X. High Q micro-ring resonators fabricated from polycrystalline aluminium nitride films for near infrared and visible photonics. *Opt. Express* **20**, 12261–12269, http://www.opticsexpress.org/abstract.cfm?URI=oe-20-11-12261, https://doi.org/10.1364/OE.20.012261 (2012).
11. Pernice, W. H. P., Xiong, C., Schuck, C. & Tang, H. X. Second harmonic generation in phase matched aluminum nitride waveguides and micro-ring resonators. *Appl. Phys. Lett.* **100**, 223501, https://doi.org/10.1063/1.4722941 (2012).
12. Absil, P. P. *et al*. Wavelength conversion in GaAs micro-ring resonators. *Opt. Lett.* **25**, 554–556, http://ol.osa.org/abstract.cfm?URI=ol-25-8-554, https://doi.org/10.1364/OL.25.000554 (2000).
13. Ibrahim, T. A., Van, V. & Ho, P.-T. All-optical time-division demultiplexing and spatial pulse routing with a GaAs/AlGaAs microring resonator. *Opt. Lett.* **27**, 803–805, http://ol.osa.org/abstract.cfm?URI=ol-27-10-803, https://doi.org/10.1364/OL.27.000803 (2002).
14. Ciminelli, C., Dell'Olio, F., Armenise, M. N., Soares, F. M. & Passenberg, W. High performance inp ring resonator for new generation monolithically integrated optical gyroscopes. *Opt. Express* **21**, 556–564, http://www.opticsexpress.org/abstract.cfm?URI=oe-21-1-556, https://doi.org/10.1364/OE.21.000556 (2013).
15. Chao, C.-Y., Fung, W. & Guo, L. J. Polymer microring resonators for biochemical sensing applications. *IEEE J. Sel. Top. Quantum Electron.* **12**, 134–142, https://doi.org/10.1109/JSTQE.2005.862945 (2006).
16. Jung, H., Xiong, C., Fong, K. Y., Zhang, X. & Tang, H. X. Optical frequency comb generation from aluminium nitride microring resonator. *Opt. Lett.* **38**, 2810–2813, http://ol.osa.org/abstract.cfm?URI=ol-38-15-2810, https://doi.org/10.1364/OL.38.002810 (2013).

17. Kim, H.-T. & Yu, M. Cascaded ring resonator-based temperature sensor with simultaneously enhanced sensitivity and range. *Opt. Express* **24**, 9501–9510, http://www.opticsexpress.org/abstract.cfm?URI=oe-24-9-9501, https://doi.org/10.1364/OE.24.009501 (2016).
18. Burrows, C. & Lee J. San Francisco. Titanium-indiffusion waveguides, http://www.freepatentsonline.com/6567598.html (2003).
19. Bortz, M. L. & Fejer, M. M. Annealed proton-exchanged LiNbO₃ waveguides. *Opt. Lett.* **16**, 1844–1846, http://ol.osa.org/abstract.cfm?URI=ol-16-23-1844, https://doi.org/10.1364/OL.16.001844 (1991).
20. Chanvillard, L. *et al.* Soft proton exchange on periodically poled LiNbO₃ : A simple waveguide fabrication process for highly efficient nonlinear interactions. *Appl. Phys. Lett.* **76**, 1089–1091, https://doi.org/10.1063/1.125948 (2000).
21. Jackel, J. L., Rice, C. E. & Veselka, J. J. Proton exchange for high-index waveguides in LiNbO₃ . *Appl. Phys. Lett.* **41**, 607–608, https://doi.org/10.1063/1.93615 (1982).
22. Stepanenko, O., Quillier, E., Tronche, H., Baldi, P. & Micheli, M. D. Crystallographic and optical properties of Z-cut high index soft proton exchange (HISoPE) LiNbO3 waveguides. *J. Light. Technol.* **34**, 2206–2212, http://jlt.osa.org/abstract.cfm?URI=jlt-34-9-2206 (2016).
23. Rambu, A. P. *et al.* Analysis of high-index contrast lithium niobate waveguides fabricated by high vacuum proton exchange. *J. Light. Technol.* **36**, 2675–2684, https://doi.org/10.1109/JLT.2018.2822317 (2018).
24. Poberaj, G., Hu, H., Sohler, W. & Günter, P. Lithium niobate on insulator (LNOI) for micro-photonic devices. *Laser & Photonics Rev.* **6**, 488–503 (2012).
25. Siew, S. Y., Saha, S. S., Tsang, M. & Danner, A. J. Rib microring resonators in lithium niobate on insulator. *IEEE Photonics Technol. Lett.* **28**, 573–576, https://doi.org/10.1109/LPT.2015.2508103 (2016).
26. Zhang, M., Wang, C., Cheng, R., Shams-Ansari, A. & Lončar, M. Monolithic ultra-high-Q lithium niobate microring resonator. *Opt.* **4**, 1536–1537, http://www.osapublishing.org/optica/abstract.cfm?URI=optica-4-12-1536, https://doi.org/10.1364/OPTICA.4.001536 (2017).
27. Krasnokutska, I., Tambasco, J.-L. J., Li, X. & Peruzzo, A. Ultra-low loss photonic circuits in lithium niobate on insulator. *Opt. Express* **26**, 897–904, http://www.opticsexpress.org/abstract.cfm?URI=oe-26-2-897, https://doi.org/10.1364/OE.26.000897 (2018).
28. Wang, C., Zhang, M., Stern, B., Lipson, M. & Lončar, M. Nanophotonic Lithium Niobate Electro-optic Modulators. 1701.06470 (2017).
29. Liang, H., Luo, R., He, Y., Jiang, H. & Lin, Q. High-quality lithium niobate photonic crystal nanocavities. *Opt.* **4**, 1251–1258, http://www.osapublishing.org/optica/abstract.cfm?URI=optica-4-10-1251, https://doi.org/10.1364/OPTICA.4.001251 (2017).
30. Li, G. *et al.* 25gb/s 1v-driving cmos ring modulator with integrated thermal tuning. *Opt. Express* **19**, 20435–20443, http://www.opticsexpress.org/abstract.cfm?URI=oe-19-21-20435, https://doi.org/10.1364/OE.19.020435 (2011).
31. Chen, L., Wood, M. G. & Reano, R. M. 12.5 pm/v hybrid silicon and lithium niobate optical microring resonator with integrated electrodes. *Opt. Express* **21**, 27003–27010, http://www.opticsexpress.org/abstract.cfm?URI=oe-21-22-27003, https://doi.org/10.1364/OE.21.027003 (2013).
32. Chen, L., Xu, Q., Wood, M. G. & Reano, R. M. Hybrid silicon and lithium niobate electro-optical ring modulator. *Opt.* **1**, 112–118, http://www.osapublishing.org/optica/abstract.cfm?URI=optica-1-2-112, https://doi.org/10.1364/OPTICA.1.000112 (2014).
33. Jung, H., Fong, K. Y., Xiong, C. & Tang, H. X. Electrical tuning and switching of an optical frequency comb generated in aluminum nitride microring resonators. *Opt. Lett.* **39**, 84–87, http://ol.osa.org/abstract.cfm?URI=ol-39-1-84, https://doi.org/10.1364/OL.39.000084 (2014).
34. Wang, C., Zhang, M., Stern, B., Lipson, M. & Lončar, M. Nanophotonic lithium niobate electro-optic modulators. *Opt. Express* **26**, 1547–1555, http://www.opticsexpress.org/abstract.cfm?URI=oe-26-2-1547, https://doi.org/10.1364/OE.26.001547 (2018).
35. Guarino, A., Poberaj, G., Rezzonico, D., Degl'Innocenti, R. & Günter, P. Electro-optically tunable microring resonators in lithium niobate. *Nat. Photonics* **1**, 407–410 (2007).
36. Siew, S. Y., Saha, S. S., Tsang, M. & Danner, A. J. Rib Microring Resonators in Lithium Niobate on Insulator. *Ieee Photonics Technol. Lett.* **28**, 573–576 (2015).
37. Regener, R. & Sohler, W. Loss in low-finesse Ti:LiNbO₃ optical waveguide resonators. *Appl. Phys. B* **36**, 143–147, https://doi.org/10.1007/BF00691779 (1985).
38. Cardenas, J. *et al.* High coupling efficiency etched facet tapers in silicon waveguides. *IEEE Photonics Technol. Lett.* **26**, 2380–2382, https://doi.org/10.1109/LPT.2014.2357177 (2014).

Acknowledgements

Author Contributions

I.K. and J.L.T. fabricated and characterized the sample. I.K. and J.L.T. and A.P. analyzed the data and contributed to writing the manuscript.

Additional Information

Competing Interests: The authors declare no competing interests.

Publisher's note: Springer Nature remains neutral with regard to jurisdictional claims in published maps and institutional affiliations.